REPORT DOCUMENTATION PAGE

Form Approved OMB NO. 0704-0188

1. REPORT DATE (DD-MM-YYYY)	2. REPORT TYPE	3. DATES COVERED (From - To)
06-01-2020	Final Report	1-Aug-2018 - 30-Apr-2019

4. TITLE AND SUBTITLE
Final Report: Bias-Modulated Nanoscale Terahertz Linear and Nonlinear Spectroscopy

5a. CONTRACT NUMBER
W911NF-18-1-0419

5b. GRANT NUMBER

5c. PROGRAM ELEMENT NUMBER
611102

6. AUTHORS

5d. PROJECT NUMBER

5e. TASK NUMBER

5f. WORK UNIT NUMBER

7. PERFORMING ORGANIZATION NAMES AND ADDRESSES
Brown University
Office of Sponsored Projects
Box 1929
Providence, RI 02912 -9093

8. PERFORMING ORGANIZATION REPORT NUMBER

9. SPONSORING/MONITORING AGENCY NAME(S) AND ADDRESS (ES)
U.S. Army Research Office
P.O. Box 12211
Research Triangle Park, NC 27709-2211

10. SPONSOR/MONITOR'S ACRONYM(S)
ARO

11. SPONSOR/MONITOR'S REPORT NUMBER(S)
73576-EL-II.1

12. DISTRIBUTION AVAILIBILITY STATEMENT
Approved for public release; distribution is unlimited.

13. SUPPLEMENTARY NOTES
The views, opinions and/or findings contained in this report are those of the author(s) and should not contrued as an official Department of the Army position, policy or decision, unless so designated by other documentation.

14. ABSTRACT

15. SUBJECT TERMS

16. SECURITY CLASSIFICATION OF:			17. LIMITATION OF ABSTRACT	15. NUMBER OF PAGES	19a. NAME OF RESPONSIBLE PERSON
a. REPORT	b. ABSTRACT	c. THIS PAGE			Daniel Mittleman
UU	UU	UU	UU		19b. TELEPHONE NUMBER 401-863-9056

RPPR Final Report
as of 28-Jan-2020

Agency Code:

Proposal Number: 73576ELII **Agreement Number: W911NF-18-1-0419**
INVESTIGATOR(S):

Name: Daniel M. Mittleman
Email: daniel_mittleman@brown.edu
Phone Number: 4018639056
Principal: Y

Organization: **Brown University**
Address: Office of Sponsored Projects, Providence, RI 029129093
Country: USA
DUNS Number: 001785542 EIN: 050258809
Report Date: 31-Jul-2019 Date Received: 06-Jan-2020
Final Report for Period Beginning 01-Aug-2018 and Ending 30-Apr-2019
Title: Bias-Modulated Nanoscale Terahertz Linear and Nonlinear Spectroscopy
Begin Performance Period: 01-Aug-2018 **End Performance Period:** 30-Apr-2019
Report Term: 0-Other
Submitted By: Daniel Mittleman Email: daniel_mittleman@brown.edu
Phone: (401) 863-9056

STEM Degrees: **STEM Participants:** 1

Major Goals: In the last few years, imaging below the diffraction limit has become one of the most active topics in the field of terahertz science. A key development that has enabled these results is the use of a metal tip, such as the tip in an atomic force microscope (AFM). This tip can be held in close proximity (perhaps 10 nm) to a sample surface, and illuminated from the far field with terahertz radiation. The scattering of light off this tip-sample junction is sensitive to the dielectric properties of the region of the sample directly underneath the tip, so nanoscale dielectric information can be extracted from the signal.

We have recently broadened the scope of this technique to include nonlinear terahertz spectroscopy in the near field. Instead of illuminating the tip with a terahertz signal, we use a near-infrared (800 nm) femtosecond pulse as the illumination source, and measure the THz radiation generated by the sample, in the vicinity of the AFM tip. Laser THz emission microscopy (LTEM) is a well-known and powerful tool for ultrafast spectroscopy. Our new results have translated this nonlinear technique into the nanoscale, as a complementary tool to our existing THz scattering microscope.

Here, we propose an exploratory project under the Short-Term Innovative Research (STIR) program, to develop a potentially transformative advance for these existing nanoscopy tools. We will investigate the use of a DC bias applied to the AFM tip as a means for modulating the sample's properties on the nanoscale. A large static DC field can have several different effects on the photophysics of condensed matter systems. In semiconductors, DC fields can induce carrier depletion as a field effect, or carrier multiplication through avalanche charge generation. In addition, a static electric field can cause a non-resonant modification of a sample's dielectric function through the DC Kerr effect. DC fields can also cause transient alignment of molecules in solution, which could be extremely valuable for applications of THz near-field techniques to samples in the liquid state.

The first phase of our 9-month research program will involve the experimental demonstration and theoretical exploration of the basic phenomena of bias-modulated tip scattering, using well-understood samples such as featureless doped semiconductor wafers. In the second phase, once we have a firm experimental and theoretical understanding of the results, we will apply the technique to a prototype nanostructured system: semiconducting nanowires. In a vertical orientation, these nanostructures will couple strongly to the vertically oriented dipole of the AFM tip, offering the possibility of observing bias-modulated THz emission from a single nanowire. In a horizontal orientation, the bias could induce carrier transport along an axis perpendicular to the nanowire axis, which can provide access to this poorly characterized aspect of these well-studied nanostructures. This geometry could be particularly interesting in the case of core-shell nanowires, where the heterojunction runs parallel to the axis of the wire, for probing spatially resolved carrier dynamics orthogonal to the wire axis.

RPPR Final Report
as of 28-Jan-2020

Accomplishments: We have developed a quantitative model which predicts the outcome of both linear scattering and nonlinear LTEM experiments. We are now working to incorporate the effects of DC bias into this model. In the meanwhile, a manuscript describing the model, and supporting data, has been submitted for publication to Optics Express, and is currently under review. A copy of this manuscript is included as an upload with this final report.

Training Opportunities: Angela Pizzuto - PhD student
Angela used the data acquired during the grant period as the basis for her qualifying exam (which she passed).

Results Dissemination: Manuscript in review at Optics Express
(see uploaded document)

Honors and Awards: Nothing to Report

Protocol Activity Status:

Technology Transfer: Nothing to Report

PARTICIPANTS:

Participant Type: Graduate Student (research assistant)
Participant: Angela Pizzuto
Person Months Worked: 4.00 **Funding Support:**
Project Contribution:
International Collaboration:
International Travel:
National Academy Member: N
Other Collaborators:

Nanoscale Laser THz Emission Microscopy and THz Nanoscopy

ANGELA PIZZUTO,[1] DANIEL M. MITTLEMAN,[2] AND PERNILLE KLARSKOV[3*]

[1]*Department of Physics, Brown University, Providence, RI 02903, USA*
[2]*School of Engineering, Brown University, Providence, RI 02903, USA*
[3]*Department of Engineering, Aarhus University, Finlandsgade 22, 8200 Aarhus N., Denmark*
**klarskov@eng.au.dk*

Abstract: We present an experimental and theoretical comparison of two different scattering-type scanning near-field optical microscopy (s-SNOM) based techniques in the terahertz regime; nanoscale reflection-type terahertz time-domain spectroscopy (THz nanoscopy) and nanoscale Laser Terahertz Emission Microscopy (LTEM). We show that complementary spectroscopic information can be gained from these techniques when employed back-to-back. For the specific case of THz nanoscopy and the LTEM imaging performed on a lightly p-doped InAs sample, we are able to record waveforms modulated up to the 6th and the 10th harmonic of the tip oscillation frequency, and measure a THz near-field confinement down to 11 nm. A computational approach for determining the spatial confinement of the enhanced electric field in the near-field region of the conductive probe is presented, which manifests an effective "tip sharpening" in the case of nanoscale LTEM due to the alternative geometry and optical nonlinearity of the THz generation mechanism. Finally, we demonstrate the utility of the finite dipole model (FDM) in predicting the scattered THz electric field, and present the first use of this model for predicting a broadband near-field response from nanoscale LTEM.

1. Introduction

In the last few decades, terahertz (THz) spectroscopy has been shown to be a powerful tool for studying charge carries in a wide variety of materials [1]. Most semiconductors have plasma frequencies in the terahertz regime, providing distinct spectral signatures in systems, which are relevant to modern electronics [2]. With a photon energy much below the band gap of conventional semiconductors, THz radiation allows for a non-invasive measurement of only the carriers, which contribute to conductivity. THz time-domain spectroscopy (THz-TDS) and imaging are well-established techniques in which the electric field of the THz pulses are detected in the time domain, preserving all spectral information [3-5]. THz-TDS can provide a quantitative characterization of a semiconductor's doping profile [6], but with a limited spatial resolution due to the diffraction limit. Thus, conventional THz techniques are not able to spatially resolve nanostructures, although THz spectroscopy can reveal the average changes in the electrical properties of a collection of nanostructures, such as semiconductor nanowires [7]. In an effort to overcome the diffraction limit and extract information about individual nanostructures, THz imaging has been adapted to various types of near-field microscopy techniques [8-15]. In one promising approach, the incoming radiation encounters a sharp metal tip that confines the probing spot to an area of size on the order of the tip diameter known as scattering-type Scanning Near-field Optical Microscopy (s-SNOM) [16, 17]. This method allows for a significant background suppression by performing lock-in detection referenced to harmonics of the oscillation frequency of the metallic tip. In the mid-IR and THz range, researchers have used s-SNOM to demonstrate a spatial resolution down to the nanoscale [6, 18], and also for combining both a high spatial and temporal resolution [19]. With the application and development of s-SNOM within the field of THz and infrared imaging, several groundbreaking studies of physical phenomena on the nanoscale have been published [20-24]. Using an s-SNOM configuration, we recently demonstrated the nanoscale version of laser THz emission microscopy (LTEM) [25]. LTEM has previously been shown to be a powerful tool for examining photo-induced charge carrier dynamics in integrated circuits [26] and for spectroscopic studies of surfaces [27, 28]. To facilitate the extraction of the dielectric function of a sample from an s-SNOM experiment, analytical models have been developed to describe the tip-sample near-field system; most notably, the point dipole model (PDM) which represents the tip as a conductive metal sphere [16], and the finite dipole model (FDM), which represent the tip as a conductive metal prolate spheroid [29, 30]. The latter is widely used, for example in extracting local carrier concentration.

Here, we have implemented a THz-TDS system in the s-SNOM configuration along with the experimental setup for nanoscale LTEM demonstrated in [25]. This allows us to perform THz-TDS with nanometer resolution, in the same experimental configuration as nanoscale LTEM measurements; for the remainder of this discussion, we refer to

this nanoscale THz-TDS imaging technique as THz nanoscopy. To show the complementarity of the two methods, we provide a direct experimental comparison of near-field tip-based THz nanoscopy and LTEM by performing back-to-back imaging of a structured InAs surface. For the THz nanoscopy and the LTEM imaging, we are able to record waveforms modulated up to the 6th and the 10th harmonic of the tip oscillation frequency, respectively, which gives an extremely tight confinement of the THz fields in both cases. To support our experimental results, we implement a computational approach for precisely determining the local field confinement in each case. Finally, we demonstrate the broad-spectrum applications of the FDM for THz nanoscopy, and the first use of the FDM for predicting THz pulses generated from nanoscale LTEM.

2. Setup

The experimental setup is illustrated in Fig. 1, and is based on a Ti:Sapphire femtosecond (fs) laser providing near-infrared (NIR) laser pulses with a center wavelength of 820 nm, pulse duration of 100 fs, and a repetition rate of 80 MHz. The near-field microscope is a commercial Atomic Force Microscopy (AFM) based s-SNOM system (Neaspec) operated in tapping mode. The AFM probe tips (Rocky Mountain Nanotechnology) are coated with PtIr, with a conical shank approximately 80 µm long and which tapers to a rounded apex with radius of approximately 20 nm. Further details about the nanoscale LTEM technique can be found in [25].

Here, we perform THz nanoscopy and nanoscale LTEM back-to-back in immediate succession to facilitate a direct comparison of the two techniques under the same experimental conditions. For the THz nanoscopy experiments, NIR pulses are incident on a large area photoconductive emitter (Tera-SED, Laser Quantum), which generates sub-picosecond single-cycle THz pulses. These pulses are collimated with an off-axis parabolic mirror (reflected focal length: 15 mm), and then sent into the microscope with an ITO-coated beam splitter to reflect the vertically polarized THz pulses and transmit the horizontally polarized NIR pulses. The incident beams are focused onto the sample surface, directly under the tip apex using another off-axis parabolic mirror, which also collects and collimates the outgoing (including the scattered) THz pulses. For both techniques, this outgoing radiation is detected via electro-optic (EO) sampling [31] and lock-in detection referenced to the tip tapping frequency (approximately 45 kHz) or its harmonics, while the beam for the other technique is blocked. The tapping amplitude for these experiments is approximately 100 nm.

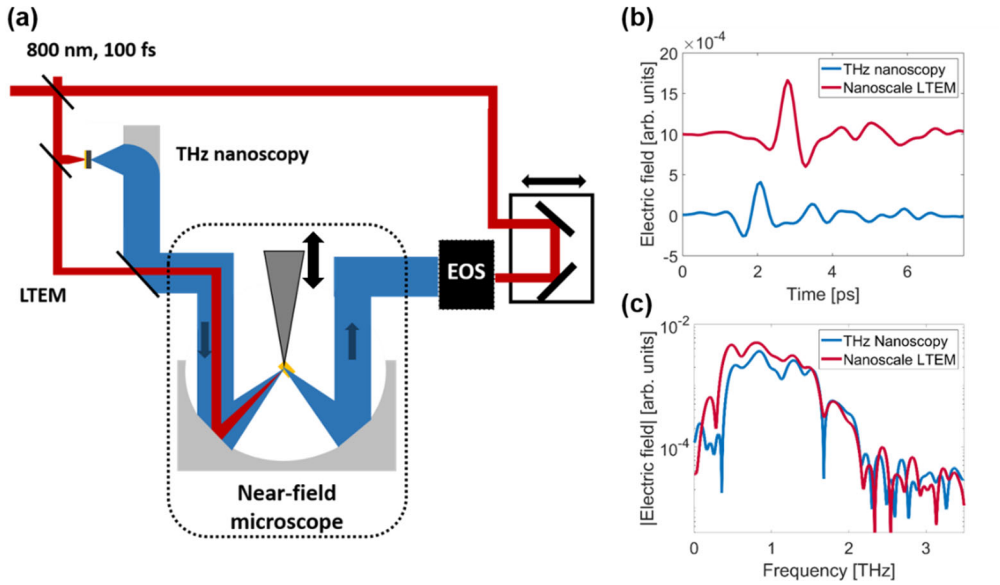

Fig. 1: (a): Schematic of the near-field experiments; NIR pulse is shown in red while the THz beam is shown in blue. A delay stage and a ZnTe EO crystal provide the coherent E-field amplitude detection. (b) Time-domain waveforms recorded with THz nanoscopy (blue) and LTEM (red) by lock-in detection to the 2nd harmonic of the tapping frequency. (c) Amplitude spectra corresponding to the recorded waveforms in (b).

The off-axis parabolic mirror located inside the near-field microscope focuses the incident THz or NIR beam to a spot whose size is approximately diffraction-limited and therefore significantly larger than the ~20 nm tip apex. As a result, a large portion of the light does not interact at all with the tip-sample system, and a significant background contribution with no near-field information is introduced. As first demonstrated by Knoll et al. [16], this background can be distinguished from the near-field signal by a Fourier decomposition of the signal strength vs tip-sample

distance, since the two contributions vary differently with tip-sample separation. Experimentally, this corresponds to demodulating our lock-in detection to higher harmonics of the tapping frequency. Higher-order harmonics increasingly isolate the near-field signal, suppressing the background more effectively at the expense of signal-to-noise. As shown below, we are able to detect near-field signals even up to the 6th harmonic of the tapping frequency (for THz nanoscopy) and the 10th harmonic (for nanoscale LTEM). However, we have found that, at least for the experiments shown here, the 2nd and 3rd harmonics are generally sufficient for discriminating the near-field information from the background, and thereby obtain a sufficiently high spatial resolution comparable to the tip diameter.

The EO sampling technique allows for coherent, time-resolved detection of the THz electric field; we may keep the sample at a fixed location while recording the waveforms as shown in Fig. 1(b), here modulated to the 2nd harmonic of the tip oscillation. In this case, we retain all spectroscopic information; Fig. 1(c) shows an example of the obtained amplitude spectra. For recording images as shown below, we instead keep the delay stage at a fixed position to measure the THz peak electric field and raster-scan the sample, generating a 2D map of the THz nanoscopy or LTEM signal. In either case, the sample topography is recorded simultaneously, which also gives the possibility to ensure that the same spatial region is imaged for each experiment. All images and time-traces shown here are recorded under ambient conditions with a lock-in time-constant of 100 ms.

3. Results

3.1 Imaging with THz Nanoscopy and Nanoscale LTEM

To rigorously compare the THz nanoscopy and nanoscale LTEM methods, we image a 3.5 µm x 3.5 µm area of a structured, lightly p-doped ($n \approx 10^{16}$) InAs sample. In Fig. 2, we show the images recorded when referencing to the 2nd harmonic of the tapping frequency. The AFM topography images recorded for both experiments appear identical, so we only show one of them here. As seen in Fig. 2(a), a groove in the surface of the InAs sample is imaged with a total height variation of 95 nm. A clear contrast is observed in both the THz nanoscopy and LTEM images shown in (b) and (c), which are plotted on the same false-color scale for the measured THz peak electric field. Considering these, a slightly higher contrast is seen for the LTEM image. As described in [25], the THz generation mechanism which is expected to be responsible for the nanoscale LTEM signal obtained from a lightly p-doped InAs sample is the photo-Dember effect [32-34].

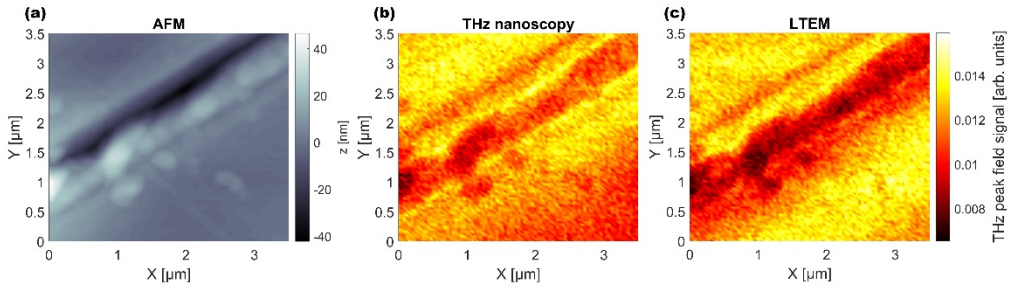

Fig. 2 Images recorded of a groove in an bulk InAs surface. (a) AFM image recorded over an area of 3.5 x 3.5 µm^2 with associated scale bar on right. (b) Peak THz Nanoscopy signal. (c) Peak LTEM signal. Associated color scale for (b), (c), is shown on the right of (c).

To study the contrast deviations of the THz nanoscopy and the LTEM techniques further, Fig. 3(a) and (b) show the two images shown in Fig. 2(b) and (c) superimposed onto their corresponding topography. Although the material is uniform bulk InAs, the strength of the signal will be highly dependent on the tip-sample distance - which may change slightly as the scans over a rapidly-changing height profile - and the presence of extra reflections. It can be seen in Figs. 2(b), 2(c) and 3(a), 3(b) that both images exhibit a bright band inside the groove. This narrow crevice may generate extra reflections and/or additional field enhancement in the vicinity of the tip. However, once the tip scans past the groove and returns to a flat region, we observe remarkably different signal behavior. This can be seen clearly in Fig. 3(c), which shows line cuts perpendicular to the groove, averaged over a uniform stripe with a width of 1.6 µm. The THz nanoscopy signal shows a local maximum just before and after the groove, with a decrease in magnitude in the flatter regions. Meanwhile, the LTEM signal is strongest far from the groove and exhibits local minimum at the rightmost groove edge.

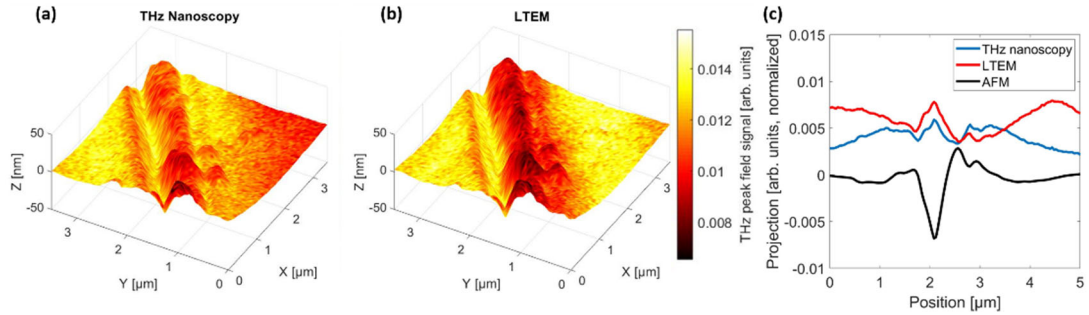

Fig. 3. (a) THz nanoscopy and (b) LTEM image superimposed on the AFM topography. (c) Projections onto a plane perpendicular to the groove of the data in a center region of the image (1.6 x 5 μm^2).

Although a rigorous theoretical approach to tip-based LTEM is yet to be developed, the differences in signal behavior between THz nanoscopy and LTEM relative to local topography emphasize that the two techniques yield complementary spectroscopic information. The nanoscale LTEM technique is anticipated to be highly sensitive to the mobility of the carriers in the subsurface of the sample responsible for the THz generation [25, 33], while the THz nanoscopy is expected to be predominantly sensitive to the local scattering properties of the surface due to its dielectric function, topography or even surface contamination. We expect that the latter is responsible for the drop in signal for the THz nanoscopy images at the rightmost side of the groove.

3.2 Higher harmonics

In early s-SNOM results using mid-IR sources, Knoll and Keilmann demonstrated the ability to discriminate the near-field signal from the background to a greater extent when referencing to a higher harmonic of the tip oscillation frequency [16]. Here, we evaluate the near-field confinement of the THz fields obtained from THz nanoscopy and nanoscale LTEM for different harmonic orders.

Figure 4 depicts the same groove as in Figs. 2 and 3, with the THz peak LTEM signal recorded with the lock-in referenced to the 1st, 2nd, 3rd, and 4th harmonics of the tip tapping frequency. We observe a sharpening of the imaged feature when the harmonic is increased; this suggests an increased spatial resolution, but at the expense of a decrease in the signal-to-noise with increasing harmonic order. The contrast at the 4th harmonic is very small although it should be noted that the THz peak field signal here is still above the noise floor. The THz nanoscopy images recorded at higher harmonics (not shown here) show a similar trend. Evidently, for samples with features in this size range (~100 nm or larger), the 2nd or 3rd harmonic are acceptable choices for sufficient background suppression.

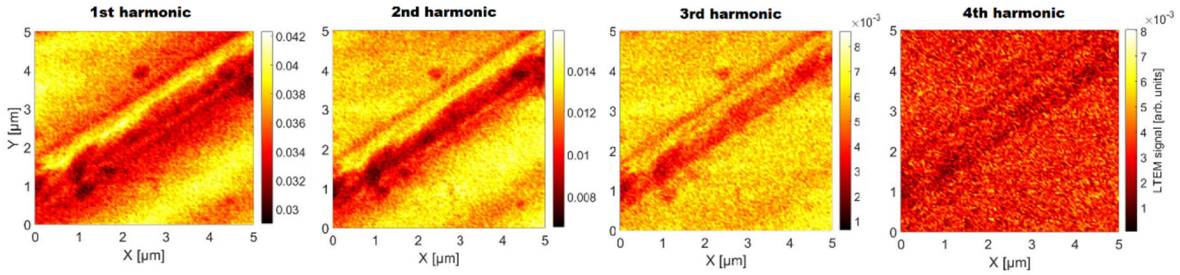

Fig. 4. Recorded LTEM images from 1st to 4th harmonic.

Although no image contrast for either technique was observed at harmonics higher than the 4th, it was still possible to record THz electric fields for higher harmonics. To study the limitations of the measurable harmonics, a fixed sample position in the upper left corner of Fig. 2 was chosen since the topography here is flat and both the LTEM and the THz nanoscopy signals are relatively high. Figure 5(a) shows the waveforms of the THz pulses recorded at the lowest (solid curves) and the highest (dotted curves) harmonic orders; these were the 6th harmonic for the THz nanoscopy measurement (blue curves) and the 10th harmonic for the LTEM measurement (red curves). We plot the peak-to-peak values of the THz pulses recorded at all measured harmonic orders in Fig. 5(b). An approximately exponential decay is observed for both LTEM and THz nanoscopy, with a slightly faster decay for the latter. The black curves in Fig. 5(b) represent our theoretical prediction, as discussed below.

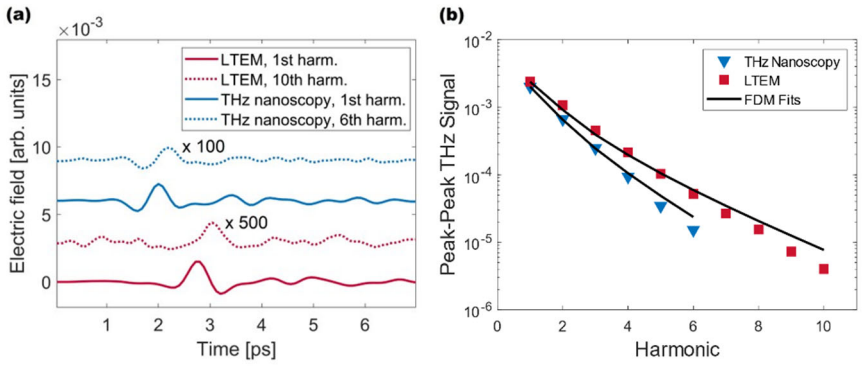

Fig. 5. (a) Waveforms of the lowest (solid lines) and highest (dotted lines) detectable harmonics for LTEM (red) and THz nanoscopy (blue). (b) THz peak-peak signal of all detectable harmonics.

Confinement of the THz electric field below the AFM tip is a key element for obtaining an image resolution that is comparable to the diameter of the tip. To estimate the THz field confinement, we measured approach curves on the same fixed sample position, in which the LTEM or THz nanoscopy peak electric fields are measured as the tip-sample distance z is increased. A pure near-field signal should decay exponentially in the region where $0 \leq z \leq r_{tip}$, and eventually taper off to a noise-limited background when the tip is far enough away from the sample surface. This behavior is shown as an example for LTEM at the 1st (red) and 5th (gray) harmonic in Fig. 6(a). The field confinement is defined as the 1/*e* width of the approach curves; double-exponential fits are exploited for an experimental estimation of this parameter (the solid lines). The double exponential fits represent both a quickly decaying term and a slowly decaying term, a reasonable method for lower harmonics (1st, 2nd) where a slowly-decaying background is observed. However, this background is effectively suppressed at higher harmonics, leaving only the quickly decaying near-field signal.

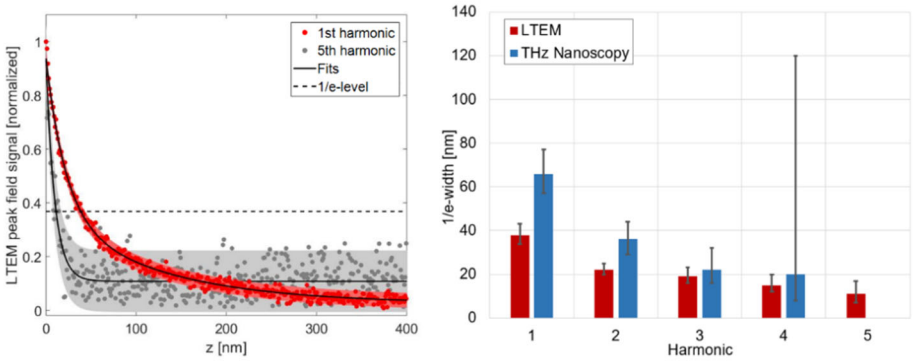

Fig. 6. (a) Double exponential fits (black solid lines) to the approach curve recorded for the 1st (red dots) and 5th (gray dots) harmonics of the LTEM peak field signal together with the associated 95% confidence interval (shaded areas). The dashed line black line shows the 1/e-level of where there field confinement is estimated. (b) Field confinements estimated as shown in (a) from all harmonic approach curves for LTEM and THz nanoscopy. Error bars are estimated from the 1/e-level of the confidence intervals.

Using these fits, we determine the 1/*e* width and the associated error bars from the 95% confidence intervals, shown as the shaded areas in transparent colors in Fig. 6(a). These are shown for both the THz nanoscopy (blue bars) and LTEM (red bars) in Fig. 6(b). For THz nanoscopy, the background noise approaches the 1/*e* level for the 4th harmonic, yielding a significant error bar for the 1/*e* width. For this reason, it was not possible to measure the field confinement for THz nanoscopy at higher harmonics. In both cases, the confinement tightens for higher-harmonic demodulation, but we observe the 1/*e* width to be significantly smaller at all harmonics for LTEM than for THz nanoscopy. We interpret this as an illustration of one of the key advantages of the nanoscale LTEM technique: having the THz source within the sample, and hence, in a much closer proximity to the tip, results in a much stronger coupling of the THz field to the tip.

The confinement estimates shown in Fig. 6(b) are listed in table 1. For the 2nd harmonic measurement for the LTEM signal, the field confinement is already comparable to the expected tip diameter (~ 20 nm); this is the case for the 3rd harmonic measurement of the THz nanoscopy signal. The tightest field confinement of 11 nm is observed for

the 5th harmonic of the LTEM signal; this is well below the expected tip diameter, even considering the error bars from the confidence interval (8 nm / 17 nm), which here are heavily influenced by the low signal-to-noise.

Table 1. Field confinements estimated from the 1/e-widths.

	THz nanoscopy [nm]		LTEM [nm]	
Harmonic	Fit	Confidence interval (lower/higher)	Fit	Confidence interval (lower/higher)
1	67	(58/78)	40	(35/45)
2	38	(32/46)	24	(22/27)
3	22	(16/32)	20	(17/23)
4	20	(8/110)	15	(12/20)
5	-	-	11	(8/17)

3.3 Theoretical approach

With the approach curves obtained above for THz nanoscopy and LTEM, we develop a theoretical framework to explore the impact of the different nature of the two methods. An electrostatic approach can be used to analytically describe the near-field interaction between the probe, sample, and incident radiation. The FDM [29] approximates the AFM tip as a conducting spheroid illuminated by a uniform electric field as illustrated in Fig. 7. The analysis below is based on the FDM as reported in [29].

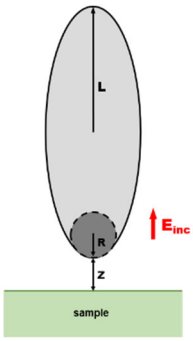

Fig. 7. Conductive spheroid approximation used within the FDM (solid line) and conductive sphere approximation used in the PDM [2] (dashed line). Selected parameters of the FDM include the spheroid semi-major axis L, the apex radius of curvature R, the tip-sample separation z, and the magnitude of the uniform external field E_{inc}.

In the far-field, the scattered electric fields are proportional to the incident field i.e. $E_{sca} \propto \alpha_{eff} E_0$, where α_{eff} is the effective polarizability

$$\alpha_{eff} = R^2 L \frac{\frac{2L}{R} + \ln\frac{R}{4eL}}{\ln\frac{4L}{e^2}} \left[2 + \frac{\beta\left(g - \frac{R+z}{L}\right)\ln\frac{4L}{4z+3R}}{\ln\frac{4L}{R} - \beta\left(g - \frac{3R+4z}{4L}\right)\ln\frac{2L}{2z+R}} \right] \quad (1)$$

where L is the half-length of the spheroid, R is the spheroid's radius of curvature at its apex, and z is the tip-sample separation. These parameters' geometric significance is shown in Fig. 7. The parameter g represents the proportion of total charge induced on the conductive ellipsoid which is concentrated near the apex, and which therefore participates in the near-field interaction.

The expression for α_{eff} contains the sample material's frequency-dependent dielectric function within the parameter $\beta = \frac{\varepsilon(\omega)-1}{\varepsilon(\omega)+1}$ and is therefore, in general, complex. Previous applications of these analytical models have been limited to a single frequency, with a continuous-wave light source in mind. We demonstrate the FDM's utility for predicting a broadband response as appropriate for pulsed THz sources in a THz-TDS system. The dielectric function of our sample (lightly p-doped InAs, $n \approx 3\times10^{16}\,cm^{-3}$) can be described with the Drude model,

$$\varepsilon(\omega) = \varepsilon_{\infty}\left(1 - \frac{\omega_p^2}{\omega^2 - i\gamma\omega}\right) \tag{2}$$

where ω_p is the material's plasma frequency, defined by

$$\omega_p^2 = \frac{n^2}{\varepsilon_0 \varepsilon_{\infty} m_{eff}} \tag{3}$$

and where $\gamma = e(m_{eff}\mu)^{-1}$ is the carrier-dependent damping parameter [35, 36]. With this dielectric function as an input, the FDM can be used to predict the relative amplitudes of the scattered electric fields at a range of frequencies and for any harmonic of the AFM tapping frequency. Using known electronic properties of our sample material, we calculate the dielectric function of the sample at each frequency, which is contained within the spectrum of the measured THz pulse. With *R*, *L*, and *g* kept as tunable parameters, we then calculate a single-frequency as a function of tip-sample distance *z*. Then, assuming a harmonic variation in *z*, we can Fourier decompose this effective polarizability, and use the resulting Fourier coefficients to determine the relative strengths of each harmonic's near-field amplitude contribution. This procedure is repeated across all frequencies, to give a series of complex scaling factors which span the entire bandwidth of our pulse, and which relate the strength of the 1st harmonic amplitudes to those of higher harmonics. Using the experimentally obtained 1st harmonic pulse as a calibration, we use this model to calculate the spectral behavior of all other harmonics and predict the shape and strength of the higher-harmonic pulses in the time domain. Predictions for the pulses' peak-to-peak amplitudes are shown as the black lines in Fig. 5(b). The excellent agreement between the measured and the predicted signals confirms the feasibility of the FDM to describe our data obtained with THz nanoscopy.

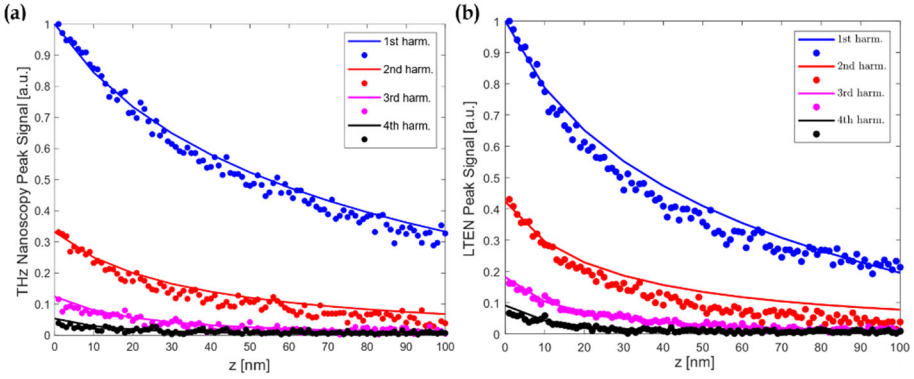

Fig. 8. Theoretical approach: Experimental (dots) and FDM predicted (solid lines) 1st, 2nd, 3rd, and 4th harmonic-demodulated approach curves are shown for THz Nanoscopy (a) and LTEM (b). These curves, representing the peak amplitude of the THz waveform in the time domain, are all normalized to peak in-contact signal at 1st harmonic demodulation.

Tunable parameters are introduced when describing the dimensions of the ellipsoid which represents the AFM probe, as well as the ellipsoid's charge distribution, induced by the external THz field. These parameters are not known *a priori*; indeed, it has been shown that the dimensions of the hypothetical ellipsoid do not correspond directly with the tip shank geometry, in general [29]. For a THz nanoscopy experiment with the known tapping amplitude of 103 nm as used above, we determine through manual tuning that the FDM very accurately recreates the THz

nanoscopy approach curves using values of L = 485 nm, R = 20 nm, and $g = 0.9e^{0.06i}$. A small complex contribution is included in g to describe the slight phase shift induced by radiation resistance and finite probe conductivity, as in prior studies [29]. This agreement is shown in Fig. 8(a). Here, the fits based on our model are shown as the solid lines together with the corresponding measured data points.

In addition to expanding the utility of this model to apply for pulsed THz sources rather than single-frequency sources, we also examine the case of nanoscale LTEM, where the THz pulses emitted by our sample via the Photo-Dember effect [25]. We again find the FDM provides accurate predictions of the emitted THz signal, both as a function of harmonic demodulation order (Fig. 5(b)) and as the tip-sample distance is increased (Fig. 8(b)). However, we note that the ellipsoid fit parameters must be adjusted in the case of nanoscale LTEM. We find that the values L = 305 nm and R = 10 nm are best for optimizing the fits in Fig. 8 (using the same value for g as noted above). We note that both of these values are smaller than those required to describe the THz nanoscopy measurement in Fig. 8(a). This apparent "tip sharpening" effect is likely due to the fact that the nanoscale LTEM experiment involves a nonlinear optical interaction at the tip apex. The THz nanoscopy interaction involves purely elastic scattering and is linear with the electric field; however, LTEM is a nonlinear process involving frequency conversion from the input 800 nm pulse to the outgoing THz pulse. It has been shown that the THz field strength from the Photo-Dember effect in InAs is linear with the incident NIR power (i.e., a quadratic nonlinearity) when observed outside a s-SNOM configuration [37]. In a tip-based approach, the complicated form of α_{eff} introduces an additional nonlinear relationship between the input power (linear with carrier density) and the strength of the coupling between the subsurface THz dipole to the AFM probe. However, we have determined to the extent of our measurement precision that the LTEM electric field strength and the NIR input power are approximately linearly related below a saturation threshold (about 50mW) [25]. We perform our experiments at power levels well below this limit, and therefore suggest that nanoscale LTEM can be understood in the context of the inherently linear FDM by considering it a second-order nonlinear process. The best-fit spheroid geometry in the THz nanoscopy case should also be accurate in representing the LTEM case if we instead examine the behavior of the *squared* E field. We substantiate this notion by performing frequency-domain finite-element (FD-FEM) simulations at an example frequency of 1 THz; results are shown in Fig. 9. Here, we show the vertical component of the electric field E_z for a tip of R = 10 nm and L = 305 nm (Fig. 9(b)), and the vertical squared electric field $|E_z|^2$ for a tip of R = 20nm and L = 485 nm (Fig. 9(c)), extracted from simulations. We extract the line profiles as shown in Fig. 9(a) and observe that the confinement profiles for these two cases are nearly identical in the highest-field region very close (within 10 nm) to the tip apex, where most of the near-field behavior originates. This similarity supports the idea that the differing fit parameters originate from the dominantly 2nd-order nonlinear THz generation mechanism in the case of nanoscale LTEM.

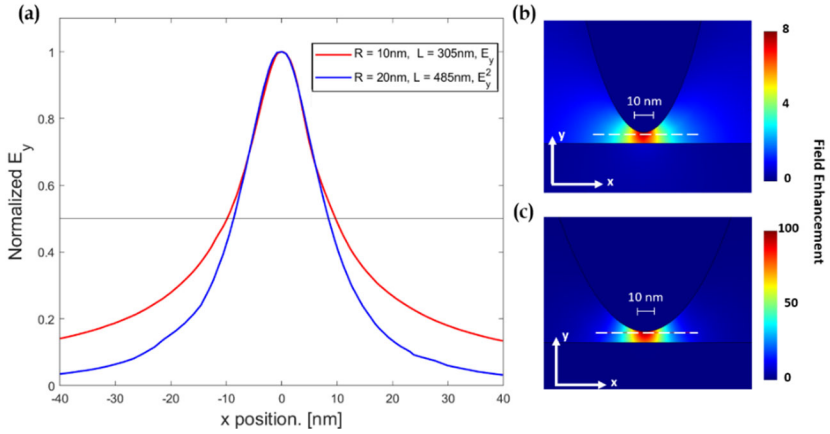

Fig. 9. (a) Line profiles of 1 THz vertical E-field enhancement from FEM simulation under conductive tip; R= 10nm and L = 305nm ellipsoid E_y indicated by the red solid line, R = 20nm and L = 485nm E_y^2 indicated by blue solid line. Profiles are normalized to same height to depict confinement width. (b) and (c) show R=10 nm, L = 305nm and R = 20nm, L = 485nm simulations, respectively. Line profiles are extracted along white dashed lines. X-y axes are shown in white.

4. Conclusions

We have experimentally demonstrated a back-to-back comparison of THz nanoscopy and nanoscale LTEM, using p-InAs as a prototypical sample for obtaining both THz time-domain waveforms and images. We have obtained a slightly better contrast for the nanoscale LTEM images and detected measurable signals at harmonic orders as high as the 10th harmonic of the tapping frequency. From the recorded approach curves, we have also extracted the field

confinement of the measured THz peak field signals and measured a field confinement down to 11 nm (8 nm / 17 nm) for the LTEM signal modulated by the 5th harmonic. We present a mathematical approach, based on the FDM, for estimating the spatial electric field confinement in the region of the tip apex. For this, we modify the FDM to account for our broadband THz signals. We also adapt this model to the case of a nanoscale LTEM measurement. From the parameters obtained by fitting the model's predictions to our measurements for the case of nanoscale LTEM, we observe a "tip sharpening" effect, which we attribute to the different experimental geometry and the nonlinear THz generation process for LTEM versus the more commonly employed case of THz nanoscopy.

Funding

Danish Council for Independent Research (Hi-TEM project); Aarhus University Research Foundation (AUFF, starting grant); U.S. National Science Foundation; US Army Research Office.

References

1. J. Lloyd-Hughes and T.-I. Jeon, "A review of the terahertz conductivity of bulk and nano-materials," J. Infrared Millim. Terahertz Waves 33, 871-925 (2012).
2. D. Grischkowsky, S. Keiding, M. van Exter, and C. Fattinger, "Far-infrared time-domain spectroscopy with terahertz beams of dielectrics and semiconductors," J. Opt. Soc. Am. B 7, 2006 (1990).
3. M. van Exter, C. Fattinger, and D. Grischkowsky, "Terahertz time-domain spectroscopy of water vapor," Opt. Lett. 14, 1128 (1989).
4. D. M. Mittleman, M. Gupta, R. Neelamani, R. G. Baraniuk, J. V. Rudd, and M. Koch, "Recent advances in terahertz imaging," Appl. Phys. B 68, 1085-1094 (1999).
5. P. U. Jepsen, D. G. Cooke, and M. Koch, "Terahertz spectroscopy and imaging - modern techniques and applications," Laser Photon. Rev. 5, 124-166 (2011).
6. A. J. Huber, F. Keilmann, J. Wittborn, J. Aizpurua, and R. Hillenbrand, "Terahertz near-field nanoscopy of mobile carriers in single semiconductor nanodevices," Nano Lett. 8, 3766-3770 (2008).
7. H. J. Joyce, C. J. Docherty, Q. Gao, H. H. Tan, C. Jagadish, J. Lloyd-Hughes, L. M. Herz, and M. B. Johnston, "Electronic properties of GaAs, InAs and InP nanowires studied by terahertz spectroscopy," Nanotechnology 24, 214006 (2013).
8. G. Keiser and P. Klarskov, "Terahertz field confinement in nonlinear metamaterials and near-field imaging," Photonics 6(2019).
9. A. J. L. Adam, "Review of near-field terahertz measurement methods and their applications," J. Infrared Millim. Terahertz Waves 32, 976-1019 (2011).
10. S. Hunsche, M. Koch, I. Brener, and M. C. Nuss, "Thz near-field imaging," Opt. Commun. 150, 22-26 (1998).
11. N. C. J. van der Valk and P. C. M. Planken, "Electro-optic detection of subwavelength terahertz spot sizes in the near field of a metal tip," Appl. Phys. Lett. 81, 1558-1560 (2002).
12. O. Mitrofanov, M. Lee, J. W. P. Hsu, I. Brener, R. Harel, J. F. Federici, J. D. Wynn, L. N. Pfeiffer, and K. W. West, "Collection-mode near-field imaging with 0.5-THz pulses," IEEE J. Sel. Top. Quantum 7, 600-607 (2001).
13. H. Zhan, R. Mendis, and D. M. Mittleman, "Superfocusing terahertz waves below λ/250 using plasmonic parallel-plate waveguides," Opt. Express 18, 9643-9650 (2010).
14. K. Wang, D. M. Mittleman, N. C. J. van der Valk, and P. C. M. Planken, "Antenna effects in terahertz apertureless near-field optical microscopy," Appl. Phys. Lett. 85, 2715-2717 (2004).
15. V. Astley, R. Mendis, and D. M. Mittleman, "Characterization of terahertz field confinement at the end of a tapered metal wire waveguide," Appl. Phys. Lett. 95, 031104 (2009).
16. B. Knoll and F. Keilmann, "Enhanced dielectric contrast in scattering-type scanning near-field optical microscopy," Opt. Commun. 182, 321-328 (2000).
17. X. Chen, D. Hu, R. Mescall, G. You, D. N. Basov, Q. Dai, and M. Liu, "Modern scattering-type scanning near-field optical microscopy for advanced material research," Adv. Mater., e1804774 (2019).
18. S. Mastel, A. A. Govyadinov, C. Maissen, A. Chuvilin, A. Berger, and R. Hillenbrand, "Understanding the image contrast of material boundaries in IR nanoscopy reaching 5 nm spatial resolution," ACS Photonics 5, 3372-3378 (2018).
19. M. Eisele, T. L. Cocker, M. A. Huber, M. Plankl, L. Viti, D. Ercolani, L. Sorba, M. S. Vitiello, and R. Huber, "Ultrafast multi-terahertz nano-spectroscopy with sub-cycle temporal resolution," Nature Photon. 8, 841-845 (2014).
20. Z. Fei, A. S. Rodin, W. Gannett, S. Dai, W. Regan, M. Wagner, M. K. Liu, A. S. McLeod, G. Dominguez, M. Thiemens, A. H. Castro Neto, F. Keilmann, A. Zettl, R. Hillenbrand, M. M. Fogler, and D. N. Basov, "Electronic and plasmonic phenomena at graphene grain boundaries," Nat. Nanotechnol. 8, 821-825 (2013).
21. M. M. Qazilbash, M. Brehm, B. G. Chae, P. C. Ho, G. O. Andreev, B. J. Kim, S. J. Yun, A. V. Balatsky, M. B. Maple, F. Keilmann, H. T. Kim, and D. N. Basov, "Mott transition in VO_2 revealed by infrared spectroscopy and nano-imaging," Science 318, 1750-1753 (2007).
22. J. Chen, M. Badioli, P. Alonso-Gonzalez, S. Thongrattanasiri, F. Huth, J. Osmond, M. Spasenovic, A. Centeno, A. Pesquera, P. Godignon, A. Z. Elorza, N. Camara, F. J. Garcia de Abajo, R. Hillenbrand, and F. H. Koppens, "Optical nano-imaging of gate-tunable graphene plasmons," Nature 487, 77-81 (2012).
23. P. Alonso-Gonzalez, A. Y. Nikitin, Y. Gao, A. Woessner, M. B. Lundeberg, A. Principi, N. Forcellini, W. Yan, S. Velez, A. J. Huber, K. Watanabe, T. Taniguchi, F. Casanova, L. E. Hueso, M. Polini, J. Hone, F. H. Koppens, and R. Hillenbrand, "Acoustic terahertz graphene plasmons revealed by photocurrent nanoscopy," Nat. Nanotechnol. 12, 31-35 (2017).
24. M. A. Huber, F. Mooshammer, M. Plankl, L. Viti, F. Sandner, L. Z. Kastner, T. Frank, J. Fabian, M. S. Vitiello, T. L. Cocker, and R. Huber, "Femtosecond photo-switching of interface polaritons in black phosphorus heterostructures," Nat. Nanotechnol. 12, 207-211 (2017).

25. P. Klarskov, H. Kim, V. L. Colvin, and D. M. Mittleman, "Nanoscale laser terahertz emission microscopy," ACS Photonics 4, 2676-2680 (2017).
26. T. Kiwa, M. Tonouchi, M. Yamashita, and K. Kawase, "Laser terahertz-emission microscope for inspecting electrical faults in integrated circuits," Opt. Lett. 28, 2058-2060 (2003).
27. F. R. Bagsican, A. Winchester, S. Ghosh, X. Zhang, L. Ma, M. Wang, H. Murakami, S. Talapatra, R. Vajtai, P. M. Ajayan, J. Kono, M. Tonouchi, and I. Kawayama, "Adsorption energy of oxygen molecules on graphene and two-dimensional tungsten disulfide," Sci. Rep. 7, 1774 (2017).
28. Y. Sakai, I. Kawayama, H. Nakanishi, and M. Tonouchi, "Polarization imaging of imperfect m-plane GaN surfaces," APL Photonics 2, 041304 (2017).
29. A. Cvitkovic, N. Ocelic, and R. Hillenbrand, "Analytical model for quantitative prediction of material contrasts in scattering-type near-field optical microscopy," Opt. Express 15(2007).
30. A. A. Govyadinov, I. Amenabar, F. Huth, P. S. Carney, and R. Hillenbrand, "Quantitative measurement of local infrared absorption and dielectric function with tip-enhanced near-field microscopy," J. Phys. Chem. Lett. 4, 1526-1531 (2013).
31. Q. Wu and X. C. Zhang, "Free-space electro-optic sampling of terahertz beams," Appl. Phys. Lett. 67, 3523 (1995).
32. P. Gu, M. Tani, S. Kono, K. Sakai, and X. C. Zhang, "Study of terahertz radiation from InAs and InSb," J. Appl. Phys. 91, 5533-5537 (2002).
33. V. M. Polyakov and F. Schwierz, "Influence of band structure and intrinsic carrier concentration on the THz surface emission from InN and InAs," Semicond. Sci. Technol. 22, 1016-1020 (2007).
34. A. Reklaitis, "Terahertz emission from InAs induced by photo-dember effect: Hydrodynamic analysis and monte carlo simulations," J. Appl. Phys. 108, 053102 (2010).
35. M. Sotoodeh, A. H. Khalid, and A. A. Rezazadeh, "Empirical low-field mobility model for III–V compounds applicable in device simulation codes," J. Appl. Phys. 87, 2890-2900 (2000).
36. A. J. Huber, D. Kazantsev, F. Keilmann, J. Wittborn, and R. Hillenbrand, "Simultaneous IR material recognition and conductivity mapping by nanoscale near-field microscopy," Adv. Mater. 19, 2209-2212 (2007).
37. R. Mendis, M. L. Smith, L. J. Bignell, R. E. M. Vickers, and R. A. Lewis, "Strong terahertz emission from (100) p-type InAs," J. Appl. Phys. 98(2005).